

Autonomous space target tracking through state estimation techniques via ground-based passive optical telescope

Peerapong Torteeka^{a,b}, Peng-qi Gao^a, Ming Shen^a, Xiao-zhong Guo^a, Da-tao Yang^a,
Huan-huan Yu^a, Wei-ping Zhou^{a,b}, Liu Tong^{a,b}, You Zhao^{a,*}

^a National Astronomical Observatories of Chinese Academy of Sciences (NAOC), No. 20B, Dutun Road, Chaoyang District, Beijing 100020, PR China

^b University of Chinese Academy of Sciences (UCAS), No. 80, Zhongguanchun-East Road, Haidian District, Beijing 100191, PR China

Received 16 March 2018; received in revised form 30 August 2018; accepted 8 September 2018

Available online 19 September 2018

Abstract

The presence of operational satellites or small-body space debris is a challenge for autonomous ground-based space object observation. Although most space objects exceeding 10 cm in diameter have been cataloged, the position of each space object (based on six orbital parameters) remains important and should be updated periodically, as the Earth's orbital perturbations cause disturbances. Modern ground-based passive optical telescopes equipped with complementary metal-oxide semiconductors have become widely used in astrometry engineering, being combined with image processing techniques for target signal enhancement. However, the detection and tracking performance of this equipment when employed with image processing techniques primarily depends on the size and brightness of the space target, which appears on the monitor screen under variable background interference conditions. A small and dim target has a highly sensitive tracking error compared to a bright target. Moreover, most image processing techniques for target signal enhancement require large computational power and memory; therefore, automatic tracking of a space target is difficult. The present work investigates autonomous space target detection and tracking to achieve high-sensitivity detection and improved tracking ability for non-Gaussian and dynamic backgrounds with a simple system mechanism and computational efficiency. We develop an improved particle filter (PF) using the ensemble Kalman filter (KF) for track-before-detect (TBD) frameworks, by modifying and optimizing the computational formula for our non-linear measurement function. We call this extended version the “ensemble Kalman PF-TBD (EnKPF-TBD).” Three sequential astronomical image datasets taken by the Asia-Pacific Ground-Based Optical Space Objects Observation System (APOSOS) telescope under different conditions are used to evaluate three proposed TBD baseline frameworks. Given an optimal random sample size, the EnKPF-TBD exhibits superior performance to PF-TBD and threshold-based unscented KF with two-dimensional peak search (2dPS). The EnKPF-TBD scheme achieves satisfactory performance for all variable background interference conditions, especially for a small and dim space target, in terms of tracking accuracy and computational efficiency.

© 2018 COSPAR. Published by Elsevier Ltd. All rights reserved.

Keywords: Telescopes; Astrometry techniques; Image processing; State estimation techniques; Atmospheric effects

1. Introduction

A development objective for modern ground-based passive optical (PO-based) space surveillance telescopes is

enhanced automatic recognition and tracking capability for real-time synergistic unresolved moving space targets (e.g., asteroids, comets, operational satellites, and space debris). For more than half a century, spacecraft technology and its applications have developed in several directions. However, the man-made objects released during space activities, including those due to the unexpected on-orbit spacecraft collision between Iridium-33 and

* Corresponding author at: National Astronomical Observatories of Chinese Academy of Sciences (NAOC), Beijing 100012, PR China.

E-mail address: youshao@bao.ac.cn (Y. Zhao).

Cosmos-2251 (Pelton, 2017), have generated an immense volume of uncontrollable fragmentation debris (1–10 cm in size), which have joined the population of resident space objects (RSOs) falling under the Kessler syndrome (Kessler et al., 2010). The volume of man-made space debris poses a growing threat to operational satellites, influencing orbital environment allocation, particularly in the low-Earth orbit regime. Furthermore, these debris items have hypervelocity relative to on-orbit (≥ 10 km/s) and slowly drifting azimuth objects, because of the effect of the Earth's perturbations. In a technical report on space debris, the United Nations Committee on the Peaceful Uses of Outer Space (Nations, 1999) has provided guidelines for space situational awareness and mitigation. Those regulations, which are devised for three primary missions for future space activities, require development of a ground- and space-based surveillance system along with implementation of mathematical modeling and orbit-removal techniques for target speed reduction and/or debris shifting to a lower orbit. However, orbit-removal techniques are still undergoing experimental research and testing.

For eventual low-cost space collision avoidance, a PO-based space surveillance telescope can be considered a practical solution to tracking, cataloging, and reducing the hazard caused by space debris among the RSOs. For the past two decades, modern near-Earth object observation telescopes have typically been equipped with monochrome high-resolution (rel. $\geq 1024 \times 1024$ pixels²) complementary metal-oxide semiconductor (CMOS) sensors that can be used to employ powerful image processing techniques. However, limited research has been performed to determine whether autonomous synergistic detection and tracking can be exploited for a space surveillance system. Traditionally, the orbital parameters of Earth-orbiting objects have primarily been provided by the North American Aerospace Defense Command (NORAD). Although space target tracking with known orbital parameters can be achieved relatively easily, knowledge of the initial orbit trajectory is required, which is obtained via human-based visual interpretation (Virtanen et al., 2016). Fully autonomous target tracking will be developed in the future, allowing progressive tracking of the increasing number of space debris items. Nevertheless, the primary challenges hindering this development are difficulties regarding moving object extraction, small and dim target detection, and the need for more robust tracking under dynamic and/or non-Gaussian backgrounds.

In the present study, we develop an autonomous space target detection and tracking technique using one of the PO-based telescopes of the Asia-Pacific Space Cooperation Organization (APSCO) space surveillance network project, named the Asia-Pacific Ground-Based Optical Space Observation System (APOSOS) project. The proposed strategy emphasizes real-time small and dim space target tracking based on non-linear and/or non-Gaussian state estimation frameworks without star sensors.

2. Background

In general, PO-based space debris astrometry establishes an orthogonal position based on a celestial coordinate system without ranging data. The CMOS sensor is the primary component, receiving sunlight reflected from space debris and fixed stars, which are identically illuminated by the Sun. However, over short periods of time, moving space debris and fixed stars have similar appearances in terms of the point spread function (PSF). Therefore, a moving space target must be distinguished against the astronomical background via image processing, with either a single image or a sequence of images being analyzed. For a high-altitude regime (\geq geosynchronous Earth orbit) and/or a small-size space target, the reflection signal has a low signal-to-noise ratio (SNR; ≤ 10 dB) with respect to the background interference.

Research towards development of an autonomous telescope system has been pursued recently, targeting combination of real-time motion detection and object tracking via a set of image sequences. Note that the image series order is always based on observation from the same stellar regime, called the STARE tracking mode. Hence, the telescope pointing angle is fixed during the observation time, which requires moving object extraction algorithms. Many investigators have recently applied state estimation algorithms based on analysis of single (Adurthi et al., 2014; Chee and Forbes, 2016; Murphy et al., 2016) or multiple images. For example, the Kalman filter (KF) and convolution mask (CM) have been combined for space target tracking using a star sensor by Ye and Zhou (2015). In this work, the zero crossing of the first derivative and the dual threshold method were used to identify the space object after removal of the astronomical background. When the space object was initially detected, the motion vectors consisting of the spatial position and velocity information were tracked by the KF. It is well known that the traditional KF is an application of the Bayes rule under the assumption that all estimates have linear, independent, and Gaussian-distributed errors. However, over a long propagation time, the system dynamics of space objects are nonlinear. Moreover, the atmospheric effects correspond to non-Gaussian interference, which presents a challenging problem for traditional optimal filtering methods.

3. Space target tracking methodology

Recent developments concerning both space and military missions have shown current capabilities for faint-target tracking, indicating variable degrees of success. One approach that may be used by space observatories is the track-before-detect framework (TBD) which, unlike alternative techniques, requires only hypotheses for extended target tracks rather than storing and processing of multiple data scans. These hypotheses are updated using the measurement detection process without a threshold

value (Rollason and Salmond, 2001). However, the primary problem is that the measurement model depends on the sensor type and interference; this is a non-linear function of the target state and directly influences the position accuracy.

PO-based autonomous space target tracking based on state estimation techniques frequently requires knowledge of the initial orbit trajectory, especially for newly observed objects. In this method, feature vectors are formed at each pixel by adding the (x, y) spatial orthogonal dimension; therefore, the characteristic of the astronomical image $(f(x, y, t))$ in each time interval (t) can be expressed using two primary terms (for the foreground and background), as follows:

$$f(x, y, t) = \underbrace{S(x, y, t)}_{\text{foreground}} + \underbrace{\vartheta(x, y, t) + \xi(x, y, t)}_{\text{background}}, \quad (1)$$

where $S(x, y, t)$ is the candidate space target in the sequence of images that can include both the fixed stars and the moving object, $\vartheta(x, y, t)$ is the astronomical or deep-space background, and $\xi(x, y, t)$ represents the unpredictable atmospheric turbulence. Normally, turbulence-induced blurring reduces image sharpness (e.g., the point corners and edges), thereby reducing the spot positioning accuracy. Then, because the image target is distributed over a larger number of pixels, the readout noise is increased. In this work, to extract the foreground moving object while suppressing the effects represented by $\xi(x, y, t)$ in Eq. (1), image retrieval and enhancement processing by means of lateral inhibition (LI) filtering is applied. This scheme can improve weak feature contrast and reduce low-frequency noise, which is beneficial for the initial orbit process, especially for small and dim space target detection with a cluttered background. In the proposed approach, the LI technique, which is discussed in more detail in Section 3.1.1, is used to provide guidance for the subsequently implemented TBD framework, as shown in Fig. 1, which illustrates the proposed autonomous space target tracking architecture.

3.1. Autonomous initial orbit trajectory

In the STARE tracking mode, most single space targets observed from the time of observation initiation ($t_{k=0}$) tend to appear in the image field of view (FoV) scanned region (Piattoni et al., 2014; Sun et al., 2015). To evaluate a novel tracking architecture, monitoring of space objects with

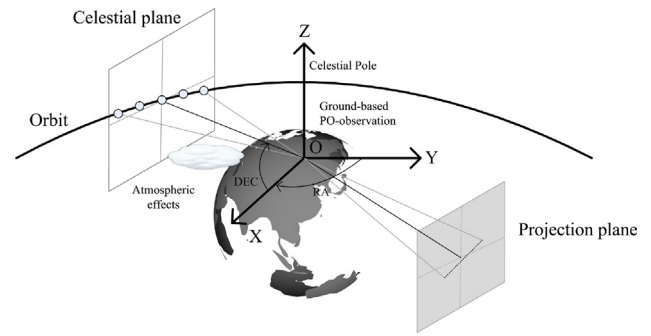


Fig. 2. Schematic of space target astrometry based on single PO-based space surveillance telescope.

known orbital parameters is prioritized. Initially, the telescope guidance system calculates the approximate candidate target position, while the two perpendicular axes of the telescope slew to the expectation point, where the target is expected to cross the image FoV within a few moments. Then, both the telescope axes are fixed. When the object crosses the FoV, the camera is operated with a short exposure time to capture the object trajectory. In the resulting image, the fixed stars and extended target have similar appearances in terms of the PSF, as shown in Fig. 2, which can be expressed in the three-dimensional Gaussian intensity distribution. The energy of the PSF-based target is usually distributed across several pixels. In the ideal case, the degree of spreading (blurring) of point-like objects is a measure of the imaging system quality. However, in real-time observation, three common situations are encountered, as shown in Fig. 3. In detail, Fig. 3(a) shows the tracking dataset (Dataset A) for a space target for a normal sky without stars. Fig. 3(b) and (c) show the tracking datasets for a small and dim space object (Dataset B) and for a space target against a highly dynamic background (Dataset C), respectively; these conditions make the detection procedure more challenging.

3.1.1. Image retrieval and enhancement

In the algorithm proposed in this work, we implement the classical spatial-based Hartline-Ratliff LI model for image retrieval and enhancement, which can be expressed as follows:

$$\mathcal{G}(x, y, t) = f(x, y, t) - \sum_{i=-A}^A \sum_{j=-B}^B \mathcal{L}_{(i,j)} \cdot f(x+i, y+j, t), \quad (2)$$

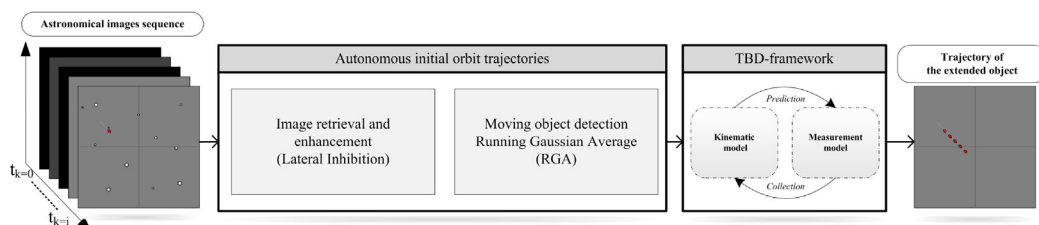


Fig. 1. Autonomous space target tracking architecture.

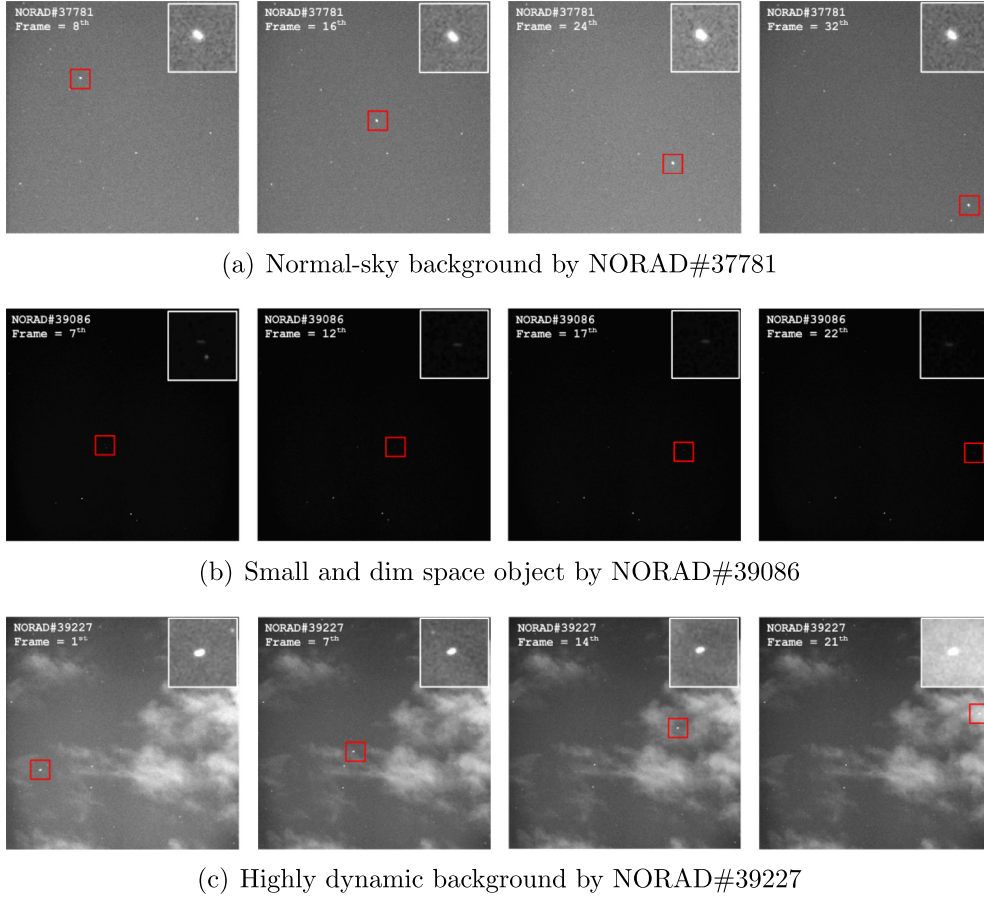


Fig. 3. (a)–(c) Tracking datasets of space targets labeled A, B, and C, respectively, with known orbital parameters. Red rectangles: Observations with 64×64 pixel² regions of interest (ROIs) around space targets. The PSF of each moving space target is shown at the top-right of the image sequence. (For interpretation of the references to color in this figure legend, the reader is referred to the web version of this article.)

where $\mathcal{G}(x, y, t)$ represents the astronomical gray value of the response output pixel and $\mathcal{L}_{(i,j)}$ is the square matrix of the LI coefficients describing the interconnections between neurons, with $[\mathcal{L}_{(i,j)}]_{(2A+1) \times (2B+1)}$. Finally, A and B represent the horizontal and vertical spread radii of the γ^{th} rings; for example, the coefficient matrix size chosen in this article is 5×5 . Then, the competing coefficient of the LI network can be expressed as

$$\mathcal{G}(x, y, t) = \mathcal{L}_{(i,j)}^{\gamma=0} \cdot f(x, y, t) - \mathcal{L}_{(i,j)}^{\gamma=1} \left[\sum_{i=-1}^1 \sum_{j=-1}^1 f(x+i, y+j, t) \right] - \mathcal{L}_{(i,j)}^{\gamma=2} \left[\sum_{i=-2}^2 \sum_{j=-2}^2 f(x+i, y+j, t) - \sum_{i=-1}^1 \sum_{j=-1}^1 f(x+i, y+j, t) \right].$$

Although there are various approaches to optimizing and balancing inhibition energy based on the mean filter, $\mathcal{L}_{(i,j)}$ should satisfy the following relationship: $\sum_{i=-A}^A \sum_{j=-B}^B \mathcal{L}_{(i,j)} = 0$. Normally, this term is adjusted based on expert knowledge and then fixed in accordance with the image sequence; however, a limitation exists in that this method is only suitable for application to a static background (Duan et al., 2013). In this work, $\mathcal{L}_{(i,j)}$ is optimized based on the Gaussian distribution model integrated with the astronomical background characteristics:

$$\mathcal{L}_{(i,j)} = \xi \cdot \exp \left(\frac{\sqrt{(x_{(i)} - x_{(i=\gamma)})^2 + (y_{(j)} - y_{(j=\gamma)})^2}}{\sigma} \right), \quad (3)$$

where ξ and σ correspond to the maximum energy ($\xi \rightarrow 1$) and decay rate $\sigma = 255/f(x, y, t)$, respectively.

3.1.2. Initial space target detection

Generally, optimal parameter estimation strategies are introduced to obtain solutions for the state-space model based on a stochastic process. However, only one state vector can be estimated at time $t_{k=1, \dots, \infty}$, $k \in \mathbb{R}^+$. To develop an autonomous system, an initial state approximation is necessary so that an expected value of the state vector $\mathbb{E}[x_t]_{(t_k=0)}$ can be obtained, before the primary tracking procedure is implemented using the TBD framework, as illustrated in Fig. 1.

To overcome the limitations of the existing intensity-based image segmentation algorithms, such as false alarms, inappropriate similarity-based segmentation, and excessive noise, the running Gaussian average (RGA) computer vision technique is applied in this work (Tang et al., 2007). This method is suitable for extracting moving

objects under dynamic and/or non-Gaussian conditions, with speed and memory being important factors (Wren et al., 1996). The traditional RGA can be expressed as follows:

$$\delta(x, y, L) = \frac{1}{L} \sum_{l=1}^L \mathcal{G}(x, y, l), \quad (4)$$

where L is the learning time, i.e., the number of frames used to construct the astronomical background model ($\delta(x, y, L)$) ordered by $l \in \mathbb{R}^+$. Here, it is assumed that an effective $\delta(x, y, L)$ is constructed in the initial stage using Eq. (4), as is common in pre-processing. After $\delta(x, y, L)$ has been constructed, we can calculate the absolute difference image ($\mathcal{D}_t^{(x,y)}$) between $\delta(x, y, L)$ and $\mathcal{G}(x, y, t)$ for each time interval ($t_{k=1, \dots, \infty}$). Hence, the Gaussian background and fixed stars can be removed, with the moving object then appearing. As regards the initial detection procedure, during the STARE tracking mode, the kinematics of the point-like space object appearing in the scene can be simply defined using a 2D spatial coordinate system incorporating the position (p_t^x, p_t^y) and velocity (v_t^x, v_t^y) with respect to the target center of mass. For long-distance space observation, the velocity of the appearing target can be considered near constant; thus, the kinematic model can simply be defined by the discrete time dead-reckoning model.

$$\begin{aligned} \begin{bmatrix} p_{t+1}^x \\ p_{t+1}^y \end{bmatrix} &= \begin{bmatrix} p_t^x \\ p_t^y \end{bmatrix} + (d_{t+1} - d_t) \cdot \begin{bmatrix} \cos(\theta_{t+1}) \\ \sin(\theta_{t+1}) \end{bmatrix}, \\ d_t &= \sum_{i=1}^k t_i \sqrt{v_{t_i}^x{}^2 + v_{t_i}^y{}^2}; \quad \theta_t = \arctan\left(\frac{v_t^y}{v_t^x}\right). \end{aligned} \quad (5)$$

Here, d_t is the accumulated target distance and θ_t is the bearing angle of the moving space target. To initialize the tracking procedure based on Eq. (5), $\mathbb{E}[x_t]_{(t=0)}$ can be determined from the $\mathcal{D}_t^{(x,y)}$ of the first two frames.

Various methods for appropriately detecting an isolated point in an image area have been proposed, six of which are used in experiment in this study to validate the performance of the proposed initial-state space target trajectory technique (Section 3.1.3). We first consider a simple potential approach using a CM, which involves moving the center of the filter mask ($\Phi_{m \times n}$), which is an odd-sized square matrix, through $\mathcal{D}_t^{(x,y)}$ from point to point. At each local point, the response of this filter is the sum of the products of the coefficient elements and the corresponding neighborhood pixels. Hence, the isolated point is detected at the location on which the mask is centered in the case of $|\Phi_{m \times n}| \geq \tau$, where τ is the non-negative threshold. The response becomes zero in an area of constant intensity. Note that processing with an odd-sized convolution matrix is appropriate, because such matrices have an unambiguous center point. Although the advantages of the CM method are its simple implementation and low time cost, its sensitivity to image interference is a disadvantage.

The Hessian measure detector Mikolajczyk and Schmid (2004) can also be used, which is based on the derivatives of

image intensity values (the corner feature detector). The minimum eigenvalues of the auto-correlation matrix that describes the gradient distribution in the local neighborhood of an isolated point can also be used to determine the significance of the signal intensity changes in the orthogonal direction (the Top-Hat and Shi-Tomasi (S&T) methods) and to then search for local maxima to localize the corner-point substitutes (Kenney et al., 2005).

The HT algorithm (Benoudnine et al., 2016) is widely used in active optical surveillance systems to solve the problem of tracking initiation due to excessive influence of measurement noise. Here, we implement circular HT, which can characterize a space target through normal parametrization of a circular shape based on the center point and radius. We also consider two-dimensional peak search (2dPS), which exploits the fact that the first derivative of a peak has a downward-going zero-crossing at the local maximum.

3.1.3. Validation experiments

To validate the performance of the proposed initial-state space target trajectory, we combined the LI filter with each of the six image-based detection algorithms mentioned above (CM, Hessian measure detector, S&T, Top Hat, HT, and 2dPS). These algorithms were used because the influence of the astronomical background is inevitable, difficult to determine based on a constant and/or accurate statistical background model in real situations, and directly affects the detection performance. Astronomers frequently consider the influence of the astronomical background as Gaussian white noise with zero mean and different standard deviations $\mathcal{N}(0, \sigma^2)$. Although this assumption is not exact, it is sufficiently accurate for the normal-sky background (Fig. 3(a)). Consequently, in this work, validation datasets covering the other two common scenarios illustrated in Fig. 3(b) and (c) were established. As noted above, the datasets corresponding to Fig. 3(a)–(c) are denoted Datasets A (36 frames), B (28 frames), and C (37 frames), respectively, with the orbit parameters listed in Table 1.

Those datasets incorporate the real astronomical background obtained by an azimuthal-mounted APOSOS telescope, stored as Flexible Image Transport System (FITS)-type gray-scale images with range $[0, 255]$. The space targets were simulated at Coordinate Universal Time, 11 Jan 2017, with observation start at 09:54:13. The APOSOS telescope specifications are listed in Table 2.

Two validation experiments were performed. The first was conducted to evaluate the image retrieval performance, for which the LI fields were selected for $[\mathcal{L}_{(5 \times 5)}]$. The image contrast, i.e., the difference between the brightest (I_{max}) and darkest (I_{min}) intensities, is one of the key indicators of image quality assessment. The image contrast measure proposed by Michelson was used here, which can be expressed as $\mathcal{C} = \frac{I_{max} - I_{min}}{I_{max} + I_{min}}$. The experimental results for the image retrieval are shown in Fig. 4(a)–(f). The three columns from

Table 1
Orbit parameters of candidate space targets.

Space target catalog number	Orbit parameters					
	Inclination	RAAN	Eccentricity	Argument of perigee	Mean anomaly	Mean motion
NORAD#37781	99.3257	140.6616	0000912	135.5591	224.5635	13.78717
NORAD#39086	98.5411	317.3127	0001721	51.6563	308.4775	14.32014
NORAD#39227	97.6122	314.7489	0001967	75.1793	55.2785	15.04511

Table 2
Specifications of 150-mm APOSOS telescope.

Item	Function	Parameters
Tube	Optical system	Aperture size: 150 mm, refractor Focal length: 500 mm Rear cut-off distance: 21 mm Image size radii: $\geq 13 \mu\text{m}$
CMOS-type	Image sensor	Resolution: $\geq 1024 \times 1024 \text{ pixels}^2$ FoV: $\geq 1.5^\circ \times 1.5^\circ$ Frame frequency: $\geq 5 \text{ frames s}^{-1}$
Mount	Support part	Track speed: $\geq 3^\circ \text{ s}^{-1}$ Track acceleration: $1\text{--}2^\circ \text{ s}^{-2}$ Position accuracy: 3–5 as Elevation range: $0\text{--}90^\circ$ Azimuth range: $0^\circ\text{--}\pm 340^\circ$
GPS	Positioning & timing service	Frequency: 10 MHz, 1 s Accuracy: 10^{-11}
IPC	Controller	Mainstream computer
Software	Observation control	Input data: NORAD-TLE data, automatic tracking Positioning: Astronomical/axial Database: Tycho-II stars catalog

left to right correspond to the normal-sky (Dataset A), small and dim space target (B), and highly dynamic background (C) cases, respectively; thus, the situation becomes more complex from left to right. In other words, it becomes more difficult to detect the space target efficiently. To analyze the pixel-based statistics (defined as gray-scale values) in a specific region of interest (ROI), image histogram analysis was used to represent the occurrence frequency of different gray-scale intensities in the specific ROI with a particular brightness value. This can be seen in Fig. 4(a)–(c), for which the order of image sequences were randomly selected at times 8, 12, and 25, for Datasets A, B, and C, respectively. Normally, a long-distance imaging target has very low energy; therefore, the target accounts for only one or a few pixels ($\approx 10 \text{ pixels}^2$) in the astronomical scene. This is the cause of the low dynamic range. From the results (Fig. 4), the LI technique reduces the effect of the dynamic background and improves the extraction performance and robustness over that of the RAW image and traditional Gaussian filtering (GF). In Fig. 4(a)–(c), the black dashed lines are the cross-sectional areas in which the space target intensities are increased by 1.891, 2.148, and 2.090 times those of the RAW image, respectively. The Michelson contrast factors after enhancement are illustrated in the statistical box plots (Fig. 4(d)–(f)), calcu-

lated for the overall pixels in the specific ROI from every frame in those datasets. The image quality assessment indicates improvement over the median values of 72% and 22% for Dataset A, and 76% and 29% for Dataset C, compared to the RAW image and traditional GF, respectively. However, the image contrast is not improved significantly in the case of Dataset B, because the standard deviation σ^2 of the background interference is very low and relatively stable. Therefore, the improvement factors of Dataset B are only 9% and 4% compared to the RAW image and traditional GF, respectively.

The second experiment determined the detection performance. Various methods for not only space target detection in the initial state, but also combination with the TBD-based state estimation frameworks have been proposed. In order to evaluate the robustness of these techniques, different levels of Gaussian background interference, with mean $\mu = 0$ and σ^2 values varying from 10^{-4} to 10^{-2} , were added to the series of RAW images in Datasets A and B. This approach was taken because the position error is directly proportional to the variance of the background interference. In addition, in this experiment, the actual space target positions were manually recognized using a human-based visual interpretation method before evaluation. Fig. 5 presents the comparative results of the six detection algorithms combined with the proposed image retrieval method. The experimental images from Fig. 5(a)–(c) illustrate the positioning errors in pixel coordinates for Datasets A–C, respectively, as measured based on the root-mean-square error (RMSE). Combined LI filtering and 2dPS yields higher positioning accuracy than the other five baseline methods for every type of astronomical dataset. Moreover, this combination works well for a small and dim target, having the highest detection probability (≥ 0.8 , Fig. 5(e)). This is because the 2dPS approach applies the weight area of the local maxima pixels.

Although both the Top-Hat and HT methods exhibit good detection performance under normal conditions (Fig. 5(a) and (d)), they are more sensitive to dim conditions and a non-Gaussian dynamic background than the other four methods. The lowest detection probability (≤ 0.2) is obtained for the Top-Hat transform for Fig. 5(f), because of the poor image quality and opacity. On the other hand, the HT technique exhibits poor performance for a small and dim object appearing with highly dynamic interference and/or under opaque conditions, as for Fig. 5(b) and (c). Both the Hessian matrix and S&T method implement the theory of second-order partial

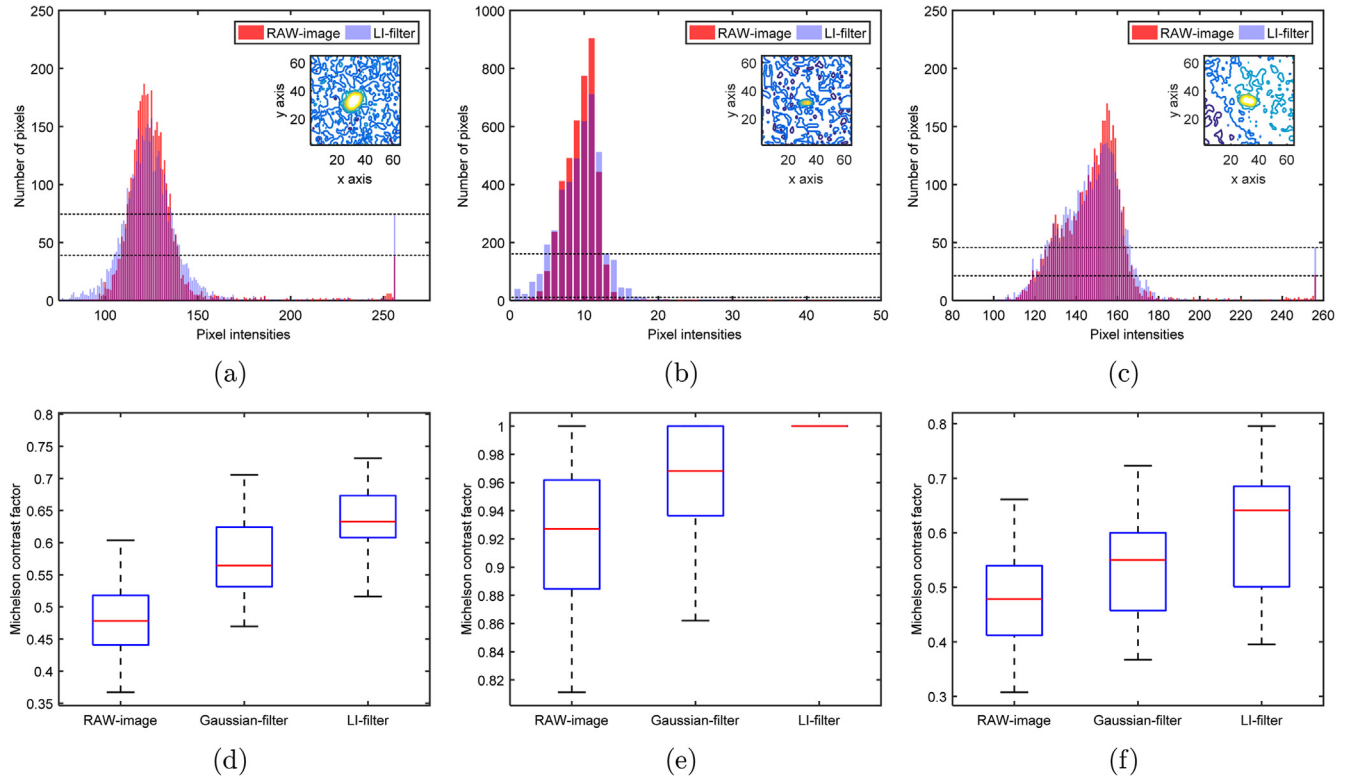


Fig. 4. (a)–(c) Comparison of image histograms for RAW and enhanced images based on LI filter for 64×64 pixel² ROI around space target, for three different situations primarily encountered in real observation: normal-sky background, small and dim space target, and highly dynamic background, respectively. The ROI-based contour on the top right of the image histogram illustrates the potential relationship between the peak value and image coordination. (d)–(f) Statistical box plots of image enhancement determined using Michelson contrast factor corresponding to three situations described above.

derivatives to find the maxima or minima of any changed area. This theory is robust, as apparent from the results shown in Fig. 5(f). We used five points at the object boundary to calculate the space-target reference position, yielding a detection probability ≥ 0.5 and near to the result for 2dPS for Dataset C. However, both the Hessian matrix and S&T techniques exhibit unstable performance for targets with features changing in only one direction. Finally, although the CM technique is not complicated and is faster than other techniques, it has low efficiency when the object is relatively insignificant; moreover, it has higher sensitivity to background interference variance, as shown in Fig. 5(b) and (e).

Based on the above results, we applied the proposed combination of LI filtering and 2dPS as the optimum approach for the time-updating process in the state estimation baseline framework.

3.2. TBD frameworks for optical space target tracking

The fundamental state-space model consists of a number of mathematical equations that describe the interactions among various state variables ($x_t \in \mathbb{R}_x^n$) throughout the physical process ($\tilde{f}(x_t)$). Although mathematical modeling provides an appropriate representation for a time-

dependent dynamic system ($T_k \triangleq t_k - t_{k-1}$), it does not yield a perfect solution without knowledge of the initial and boundary conditions, which are difficult to determine with high accuracy. Therefore, the Bayesian estimation framework with tracking for the first two moments (mean and covariance) of an assumed, known probability density function (pdf) of an initial target state $p(x_0)$ remains the conceptual design of many optimal stochastic filtering approaches (Fang et al., 2017). These techniques recursively estimate x_t from measurement data ($z_t \in \mathbb{R}_x^n$), where n_x is the dimension of the target state vector.

In this paper, we consider multiple-input and multiple-output nonlinear discrete-time stochastic process, expressed as follows:

$$x_{t+1} = \tilde{f}(x_t) + w_t, \quad (6)$$

$$z_t = h(x_t) + v_t, \quad (7)$$

where $h(x_t)$ is a known, possibly nonlinear function of the relationship between measurements and states (Huang and Hu, 2014). Further, w_t and v_t represent unknown disturbances and/or poor modeling effects of $\tilde{f}(x_t)$ and $h(x_t)$, with zero-mean and covariance Q_t and R_t respectively. Both the unknown disturbances are first assumed to be white-Gaussian and mutually independent. In order to minimize the pdf tracking of x_t by the given real measurement data-

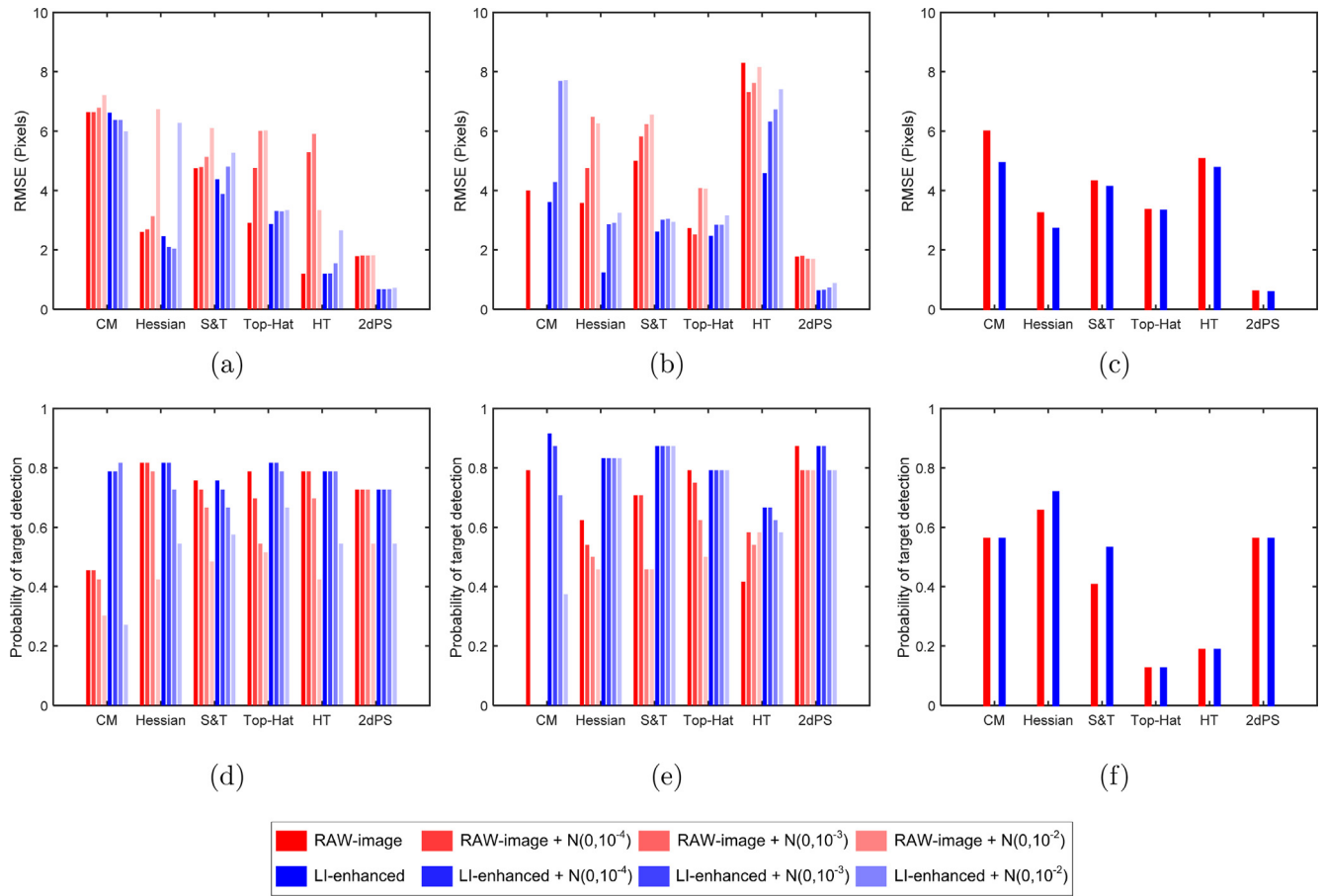


Fig. 5. (a)–(c) Comparison of six point-like detection algorithms combined with proposed LI image retrieval method, along with (d)–(f) their target detection probabilities, for three different situations encountered in real observation: normal-sky background (Dataset A), small and dim space target (Dataset B), and highly dynamic background (Dataset C), respectively. For Datasets A and B, different levels of Gaussian background interference were added.

set, we define $\mathbb{Z}_t = \{z_1, z_2, \dots, z_t\}$, denoted as $p(x_t | \mathbb{Z}_{t-1})$. According to the Bayesian estimation theory, the Bayesian recursive framework consists of two main processes, namely, prediction and correction, as illustrated in Fig. 6. The propagation of the posterior state pdf from each sam-

pling period (T_k) by $\tilde{f}(x_t)$ can be expressed using a probabilistic description, as follows:

$$p(x_t | \mathbb{Z}_{t-1}) = \int p(x_t | x_{t-1}) p(x_{t-1} | \mathbb{Z}_{t-1}) dx_{t-1}, \quad (8)$$

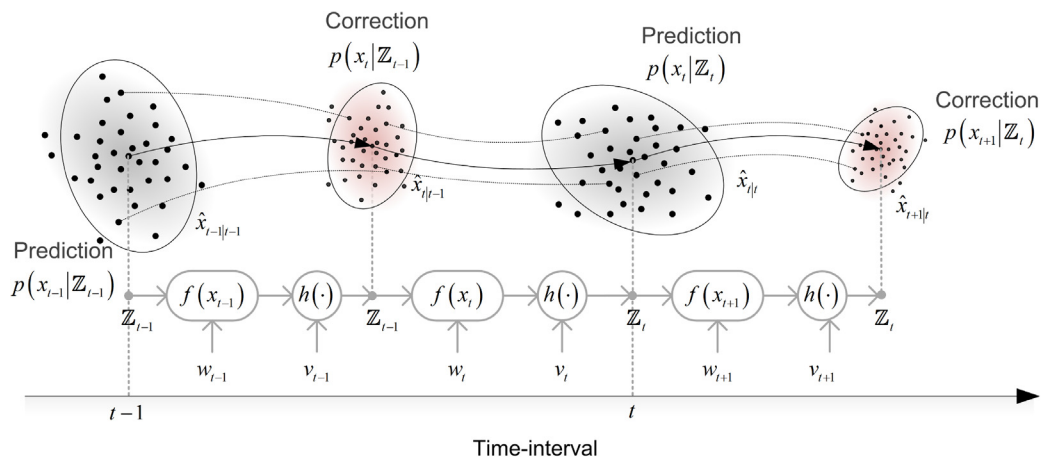


Fig. 6. Schematic of ensemble Kalman particle filter-TBD (EnKPF-TBD) algorithm.

where $p(x_t|x_{t-1})$ is the transition density and $p(x_{t-1}|\mathbb{Z}_{t-1})$ is the complete posterior pdf of state based on observation of the prior time step. Subsequently, the correction process combines the measurement data and updates the state variables to provide $p(x_t|\mathbb{Z}_t)$ at the sampling interval (t). This can be expressed as follows:

$$p(x_t|\mathbb{Z}_t) = \frac{p(z_t|x_t)p(x_t|\mathbb{Z}_{t-1})}{\Upsilon}, \quad (9)$$

where $p(z_t|x_t)$ is the likelihood of z_t based on the prediction value of x_t and $\Upsilon = \int p(z_t|x_t)p(x_t|\mathbb{Z}_{t-1})dx_t$ is the normalizing factor.

The sequential Monte-Carlo (SMC)-based particle filter (PF), developed by Gordon et al. (1993), is widely used at present. In this approach, a set of on-line posterior pdf estimations based on non-parametric techniques is used. The PF method applies a set of random samples (also called particles). When the particles are efficiently placed, weighted, and propagated, posteriors can be calculated sequentially over time. The PF-TBD framework was introduced by Salmond and Birch (2001) and has been effectively applied for PO-based stealthy target tracking under high levels of static and/or Gaussian background noise of known distribution. Although the PF-TBD framework works well for stealthy conditions, both the proposed distribution and computational complexity are disadvantages of this framework (Li and Li, 2017).

Ensemble KF (EnKF), schematically illustrated in Fig. 6, is an alternative approach based on the concept of KF combined with the SMC method. This technique often performs well for large-scale nonlinear systems and geophysical data assimilation, because linearization is not required. Moreover, the computational complexity is lower than those of both the unscented KF (UKF) Julier and Uhlmann (2004) and PF (Evensen, 2003). Comparison of the PF and EnKF performance has been reported in Bocquet et al. (2010), Nagarajan et al. (2011), and Shen et al. (2016). Obviously, a KF-based structure provides good estimates for a small ensemble number, outperforming the PF in terms of computation time. However, this method does not provide a good estimation for the posterior in a non-Gaussian environment; this is the primary limitation of EnKF. For this main reason, many researchers have recently worked to improve the EnKF by considering combination with the PF (Shen and Tang, 2015; Bi et al., 2015; Robert and Kunsch, 2016).

In this study, we also modify the EnKF and PF for a nonlinear and non-Gaussian space target tracking process based on the TBD framework, to develop an extended version that we call the “ensemble Kalman particle filter-TBD (EnKPF-TBD).” For long-range observation, the kinematic model of a moving space target projected onto a 2D spatial coordinate system (see Eq. (6)) can be defined by five state variables, with $x_t = [p^x, v^x, p^y, v^y, \Omega]^T$, where Ω_t is the intensity level of the space target. Therefore, the ensemble state variables propagate according to $\tilde{f}(x_t)$

through the sampling period of the dynamic system T_k and can be expressed as follows:

$$\hat{x}_{t|t-1}^{(i)} = \hat{f}(\hat{x}_{t-1|t-1}^{(i)}) + w_{t-1}^{(i)}, \quad i = 1, 2, \dots, N_e, \quad (10)$$

where $(\hat{x}_{t|t-1}^{(i)})$ is a prior ensemble of samples. Hence,

$$\tilde{f}(x_t) = \begin{bmatrix} 1 & T_k & 0 & 0 & 0 \\ 0 & 1 & 0 & 0 & 0 \\ 0 & 0 & 1 & T_k & 0 \\ 0 & 0 & 0 & 1 & 0 \\ 0 & 0 & 0 & 0 & 1 \end{bmatrix}, \quad Q_t = \begin{bmatrix} Q_1 & 0_{2 \times 3} \\ 0_{3 \times 2} & Q_2 \end{bmatrix},$$

$$Q_1 = \begin{bmatrix} \frac{\varphi_1}{3} T^3 & \frac{\varphi_1}{2} T^2 \\ \frac{\varphi_1}{2} T^2 & \varphi_1 T \end{bmatrix}, \quad Q_2 = \begin{bmatrix} \frac{\varphi_2}{3} T^3 & \frac{\varphi_2}{2} T^2 & 0 \\ \frac{\varphi_2}{2} T^2 & \varphi_2 T & 0 \\ 0 & 0 & \varphi_2 T \end{bmatrix}.$$

where φ_1 and φ_2 are the variances of the target acceleration and return intensity noise, respectively. From Eq. (10), the empirical mean $(\hat{x}_{t|t-1})$ and covariance $(P_{t|t-1}^x)$ of these predicted ensembles can be expressed as follows:

$$\hat{x}_{t|t-1} = \mathbb{E}(x_t|\mathbb{Z}_{t-1}) \approx \frac{1}{N_e} \sum_{i=1}^{N_e} \hat{x}_{t|t-1}^{(i)}, \quad (11)$$

$$P_{t|t-1}^x = \mathbb{C}\mathbb{O}\mathbb{V}(x_t|\mathbb{Z}_{t-1}) \approx \frac{1}{N_e - 1} \sum_{i=1}^{N_e} (\hat{x}_{t|t-1}^{(i)} - \hat{x}_{t|t-1})(\hat{x}_{t|t-1}^{(i)} - \hat{x}_{t|t-1})^T. \quad (12)$$

The correction step was initially calculated using the predicted ensembles for $p(x_t|\mathbb{Z}_{t-1})$ through Eq. (7), as follows:

$$\hat{z}_{t|t-1}^{(i)} = h^{(m,n)}(\hat{x}_{t|t-1}^{(i)}) + v_t^{(i)}, \quad i = 1, 2, \dots, N_e, \quad (13)$$

where $h^{(m,n)}(\hat{x}_{t|t-1}^{(i)})$ represents the distribution intensity of the space target in each set of observation cells $\mathcal{O}_m(\hat{x}_{t|t-1}^{(i)})$ and $\mathcal{O}_n(\hat{x}_{t|t-1}^{(i)})$, as indexed by m, n . Moreover, we assume that $v_t^{(i)}$ is independent of $w_{t-1}^{(i)}$ and has a white Gaussian distribution with zero mean and variance ε^2 .

A tracking strategy incorporating the image information in its entirety is not suitable for real-time observation, because it is time-consuming. To reduce the effect of this limitation, we can determine the specific ROI through the TBD frameworks. The space target position can be predicted using Eq. (11), where the center of a specific ROI of size 64×64 pixels² can be determined using $p_{t|t-1}^x$ and $p_{t|t-1}^y$. In addition, the signal of a space target in a specific ROI can be enhanced through RGA-based moving object extraction. Therefore, after processing by Eq. (4), we can modify the new optimal astronomical background according to $T_k(\delta_t^{(x,y)})$ using the empirical weight $(\alpha) \in [0, 1]$, which depends on the scene variability. In traditional RGA, the intensity levels of $\mathcal{D}_t^{(x,y)}$ can be classified into

three cases based on two boundary thresholds: the upper (τ_{up}) and lower (τ_{lw}) limits. This can be expressed as follows:

$$\delta_t^{(x,y)} = \begin{cases} \delta_{t_{k-1}}^{(x,y)}, & \text{if } \mathcal{D}_t^{(x,y)} \geq \tau_{up}, \\ \alpha \mathcal{G}(x, y, t) + (1 - \alpha) \delta_{t_{k-1}}^{(x,y)}, & \text{if } \tau_{lw} \leq \mathcal{D}_t^{(x,y)} \leq \tau_{up}, \\ \mathcal{G}(x, y, t), & \text{if } \mathcal{D}_t^{(x,y)} \leq \tau_{lw}. \end{cases} \quad (14)$$

Typically, α is manually adjusted according to human visual interpretation and can be observed from the scene variability. This process is complex and readjustments are time-intensive. Therefore, we automatically optimize the dynamics of the astronomical background model under the condition of the fuzzy logic algorithm, which is based on the simulation result of a previous work (Torteeka et al., 2017b). As mentioned in Section 3.1, according to the STARE tracking mode, the distribution intensity of the space target can be modeled by the PSF as a point target intensity at the rectangular position; therefore, $h^{(m,n)}(x_{t|t-1}^{(i)})$ in Eq. (13) can be defined as follows:

$$h^{(m,n)}(x_{t|t-1}^{(i)}) = \frac{\Delta_x \Delta_y \Omega_{t|t-1}}{2\pi \Sigma^2} \exp \left(-\frac{(p_{t|t-1}^x - m \Delta_x)^2 + (p_{t|t-1}^y - n \Delta_y)^2}{2\Sigma^2} \right), \quad (15)$$

where Δ_x and Δ_y are the sizes of $\mathcal{O}_m(x_{t|t-1}^{(i)})$ and $\mathcal{O}_n(x_{t|t-1}^{(i)})$ in 2D spatial coordinates. The variable Σ represents the blurring coefficient of the PSF.

In this work, we modified the EnKPF-TBD for nonlinear measurement functions; therefore, from Eq. (9), the likelihood functions of the target states are the pdf of the target existing among the background interference for each observation cell $p(z_t^{(m,n)} | x_{t|t-1}^{(i)})$, considering the target state variables based on the assumption of Gaussian measurement noise, which is independent of the pixel measurement. This can be expressed as follows:

$$p(z_t^{(m,n)} | x_{t|t-1}^{(i)}) \triangleq \frac{1}{\sqrt{2\pi\epsilon^2}} \exp \left(-\frac{(z_t^{(m,n)} - h_t^{(m,n)}(x_{t|t-1}^{(i)}))^2}{2\epsilon^2} \right). \quad (16)$$

Normally, the target's existence affects only the set of pixels around the local maximum value of its location. The expression of this case can be optimized as follows:

$$p(z_t^{(m,n)} | x_{t|t-1}^{(i)}) \approx \prod_{m \in \mathcal{O}_m(x_{t|t-1}^{(i)})} \prod_{n \in \mathcal{O}_n(x_{t|t-1}^{(i)})} p(z_t^{(m,n)} | x_{t|t-1}^{(i)}).$$

Therefore, the likelihood function of PSF-based space target existence can be defined as

$$\ell(z_t^{(m,n)} | x_{t|t-1}^{(i)}) = \prod_{m=1}^{n_l} \prod_{n=1}^{n_c} \exp \left(-\frac{h_t^{(m,n)}(x_{t|t-1}^{(i)}) [h_t^{(m,n)}(x_{t|t-1}^{(i)}) - 2z_t^{(m,n)}]}{2\epsilon^2} \right). \quad (17)$$

Here, the variables n_l and n_c are the numbers of pixels in the observation cells, which are affected by the space target intensity. Then, the ensemble weights ($\omega^{(i)}$) are normalized using Eq. (17), which can be expressed as $\tilde{\omega}^{(i)} = \omega^{(i)} / \sum_{i=1}^{N_e} \omega^{(i)}$. The ensembles $x_t^{(i)}$ are then retained by the re-sampling process according to their $\omega^{(i)}$. Subsequently, the estimated measurement data are obtained using the relation $\hat{z}_{t|t-1} = \frac{1}{N_e} \sum_{i=1}^{N_e} \omega^{(i)} \hat{z}_{t|t-1}^{(i)}$. Finally, to perform the analysis using the EnKF approach, the moving object image extracted using the RGA-fuzzy process (\bar{z}_t) can be applied to correct each member of the a priori ensembles ($\hat{x}_{t|t}^{(i)}$) using the Kalman gain ($\mathcal{K}^{(i)}$). This method is expressed as follows:

$$\hat{x}_{t|t}^{(i)} = \hat{x}_{t|t-1}^{(i)} + \mathcal{K}^{(i)} \cdot (\bar{z}_t - \hat{z}_{t|t-1}^{(i)}); \quad i = 1, 2, \dots, N_e. \quad (18)$$

Hence,

$$\mathcal{K}^{(i)} = \left\{ \frac{1}{N_e - 1} \sum_{i=1}^{N_e} [\hat{x}_{t|t-1}^{(i)} - \hat{x}_{t|t-1}] [\hat{z}_{t|t-1}^{(i)} - \hat{z}_{t|t-1}]^\top \right\} \times \left\{ \frac{1}{N_e - 1} \sum_{i=1}^{N_e} [\hat{z}_{t|t-1}^{(i)} - \hat{z}_{t|t-1}] [\hat{z}_{t|t-1}^{(i)} - \hat{z}_{t|t-1}]^\top + R \right\}^{-1}.$$

Once obtained, ($\hat{x}_{t|t}^{(i)}$) can be considered the approximation value of $p(x_t | \mathbb{Z}_t)$. The algorithm then corrects both the mean and covariance of $\hat{x}_{t|t}$, which can be expressed as follows:

$$\hat{x}_{t|t} = \mathbb{E}(x_t | \mathbb{Z}_t) \approx \frac{1}{N_e} \sum_{i=1}^{N_e} \hat{x}_{t|t}^{(i)}, \quad (19)$$

$$P_{t|t}^x = \mathbb{Cov}(x_t | \mathbb{Z}_t) \approx \frac{1}{N_e - 1} \sum_{i=1}^{N_e} (\hat{x}_{t|t}^{(i)} - \hat{x}_{t|t}) (\hat{x}_{t|t}^{(i)} - \hat{x}_{t|t})^\top. \quad (20)$$

In practical implementation of non-linear stochastic filtering conducted by the authors in previous studies, successful applications generally required adjustment of the covariance matrix (Q, R) together with the filter parameters before process implementation (Torteeka et al., 2017a; Insom et al., 2017), based on a trial-and-error method. Further, the problem of particle degeneracy in the PF exists, which relates to the scenario in which the proposed density of the prior pdf is not conditioned on the real measurement. This scenario renders almost all sample particles useless, especially for a small and dim target. The optimal framework should be selected considering not only the esti-

Table 3
List of initial parameters for autonomous PO-based space target tracking.

Functions	Model Variable Description	Symbol	Unit	Initial Value
Image retrieval & enhancement	LI coefficient matrix size	$\mathcal{L}_{(i,j)}$	Matrix square	5
	Number of frames used to construct astronomical background model	L	Frame	10
	ROI size	ROI	–	64×64
RGA-based moving object extraction	Upper limit threshold	τ_{up}	–	100
	Lower limit threshold	τ_{lw}	–	50
Initial state detection of 2dPS algorithm	Background interference threshold of Dataset A	–	Gray-scale	175
	Background interference threshold of Dataset B	–	value	35
	Background interference threshold of Dataset C	–		200
TBD tracking frameworks	Number of ensembles	N_e	Number	[300, 450]
	Number of particles	N_p	Number	[700, 900]
	Variance of target acceleration and return intensity noise	φ_1, φ_2	–	0.01, 0.001
	Observation size	$\Delta_x = \Delta_y$	–	5
	Blurring coefficient	Σ	–	0.7
	UKF + 2dPS covariance of matrix	R	–	$I_{(5 \times 5)} \times 10$

mation accuracy and computation time, but also the structural complexity. Therefore, in this study, we propose three primarily different baseline methods: (i) a novel EnKPF-TBD framework, (ii) the multiple model PF-TBD, and (iii) threshold-based UKF + 2dPS. This method is discussed in more detail in an experimental context in the next section.

4. Performance evaluation and discussion

A TBD-framework-based space target tracking experiment was conducted using an APOSOS telescope and the proposed method. The observation site of the APOSOS telescope was located at the National Astronomical Observatories of the Chinese Academy of Sciences, Beijing, China (Lat.: 40.0028, Long.: 116.3876 deg, based on WGS84). For the telescope guidance system, the TLE open-access database of orbit parameters provided by NORAD was used to calculate the orbital prediction (Liu, 1987). The astronomical image datasets acquired in this experiment cover the three primary situations encountered in space observation (Fig. 3(a)–(c)). All experiments were conducted on a personal computer with an Intel(R) Core(TM)2 Duo CPU 2.67-GHz processor and 4.0-GB memory, and all programs were implemented via MATLAB® version R2016a. Typically, the sequential astronomical background clutter is independent, both pixel to pixel and frame to frame, which can be observed from the σ^2 values, as shown in the lower sections of Fig. 8(g)–(i). Moreover, this parameter is inversely proportional to the extraction performance (Ng and Delp, 2010). In practical implementations conducted in our previous studies, the TBD tracking strategy performance was found to be directly related to the moving object extraction procedure, which is based on the updating process of the adaptive background model implemented by the observer. Following Eq. (14), we applied fuzzy logic conditions to automat-

ically balance the effects of $\mathcal{G}(x, y, t)$ and $\delta(x, y, t_{k-1})$, which can be defined by both RGA boundary thresholds, listed in Table 2. Typically, for small and dim target detection with good efficiency, the background clutter is distinctively suppressed while the target signal is enhanced.

It was necessary to validate the suppression performance indexes. The first indicator was the image signal-to-cutter ratio (SCR), representing the difficulty of small-target extraction and defined as $SCR = |\mu_{ob} - \mu_{bk}| / \sigma_{bk}^{ROI}$. Here, μ_{ob} is the average intensity of the object of interest, μ_{bk} is the average background intensity, and σ_{bk}^{ROI} is the standard deviation of the background intensity within the specified ROI, which excludes the object region. In addition, the extraction performance could also be measured using the improved SCR (ISCR), where $ISCR = SCR_{in} / SCR_{out}$. The ISCR indicates the extraction procedure enhancement with the input-image SCR (SCR_{in}) before and after processing with the output-image SCR (SCR_{out}). The background suppression factor (BSF) was also considered, where $BSF = \sigma_{in} / \sigma_{out}$. Here, σ_{in} and σ_{out} are the standard deviations of the whole-image ROI before and after processing, respectively.

For Datasets A and B, the illumination change was relatively stable. This is apparent from the σ^2 of the scatter points of the input images (red¹ circles) and extraction images (blue circles) including the fitted data (blue dashed line) in the lower sections of Fig. 8(g)–(h), showing the BSF improvement trend. Further, Fig. 8(j)–(k) give the image histogram results. As has been proven, the background interference of both cases had white-Gaussian characteristics. From the statistical data listed in Table 3, the average SCR_{out} values of Datasets A and B were 17.5768 and 11.0422, respectively. However, for Dataset C (the highly

¹ For interpretation of color in Fig. 8, the reader is referred to the web version of this article.

Table 4
PO-based space target extraction performance indexes.

Datasets	SCR _{in}			SCR _{out}			ISCR			BSF		
	Mean	Max	Min	Mean	Max	Min	Mean	Max	Min	Mean	Max	Min
A. Normal-sky background	16.3324	19.2014	7.1045	17.5768	21.2788	12.6167	1.7892	14.0479	0.9715	0.7733	0.9469	0.0773
B. Small and dim space object	10.0493	17.2060	7.3962	11.0422	17.6980	7.9366	1.1354	1.2174	1.0189	1.0314	1.1034	0.9643
C. Highly dynamic background	6.3910	8.8892	0.5597	7.6981	10.5155	4.0615	2.3569	20.3434	1.0092	0.9191	1.1364	0.6476

dynamic background), the noise was non-Gaussian (see Fig. 8(i)) and dynamically changed from frame to frame (Fig. 8(i), lower section). Note that the RGA update condition given in Eq. (14) should follow $\mathcal{G}(x, y, t)$ rapidly, to extract the moving object. Among the examined datasets, the highest average value given by the ISCR was for Dataset C, at 2.3569. Consequently, the proposed RGA-based moving object extraction can be achieved in that case (see Table 4).

We next discuss experimental evidence for the performance of the proposed TBD tracking baseline framework. Here, a moving space target was modeled based on Eq. (5). We assumed that a single moving space target appeared to cover the whole image sequence with a constant velocity, and crossed over the critically dynamic background area, as illustrated in Fig. 3(a)–(c). We used the Tycho-II star catalog to identify the fixed stars as reference positions and transformed the estimated position in 2D spatial coordinates to celestial coordinates based on the least-squares method (Kovalevsky and Seidelmann, 2004). The reference fixed stars were then recognized by $\mathcal{D}_t^{(x,y)}$. The tracking performance of the proposed TBD framework was evaluated in terms of accuracy and robustness, based on the RMSE between the true and estimated positions. Three combination algorithms were compared: the proposed EnKPF-TBD, PF-TBD, and threshold-based UKF + 2dPS. In the simulation process, both non-parametric techniques were implemented with the optimal number of random samples (for both N_e and N_p).

The results shown in Fig. 7(a) indicate the relationship between the estimation accuracy and random sample size. Although the tracking accuracy improved with the random sample size, the computation time also linearly increased, as illustrated in Fig. 7(b). However, when the number of random samples exceeded 350 and 700 for the EnKPF-TBD and PF-TBD, respectively, the estimation accuracy entered a steady state condition with a small-rate improvement, but with continually increasing computation time. The present finding appears consistent with other research (Boers et al., 2006), in which the random sample size was found to have a significant effect on the solution of every non-parametric technique, because the estimation accuracy and random sample sizes are dependent. Therefore, we must balance the estimation accuracy and efficiency for sequential moving space target images by compromising in terms of the random sample size between the end of the transient response and the beginning of the steady state response, as detailed in Table 2. Hence, the estimated accu-

racy is improved. Note that, in this evaluation, the random sample uniform proposal densities (ρ) were set to $x_{p_i^{(x,y)}} \sim \rho(-5, 5)$, $x_{v_i^{(x,y)}} \sim \rho(-2, 2)$, and $x_{\Omega_i} \sim \rho(-5, 5)$, and the probability of target existence $P_b = P_d = 0.01$, for the PF-TBD framework only.

The initial state vector of the space target was automatically detected via the 2dPS algorithm for the first two frames (as detailed in Sections 3.1.2 and 3.1.3). In the first tracking validation, we employed Dataset A, a commonly encountered scenario with a low-clutter background. The tracking performance achieved using this dataset is shown in Fig. 8(a), (d), and (g). In a comparison considering all tracking frames, the proposed EnKPF-TBD, PF-TBD, and UKF + 2dPS with background interference threshold

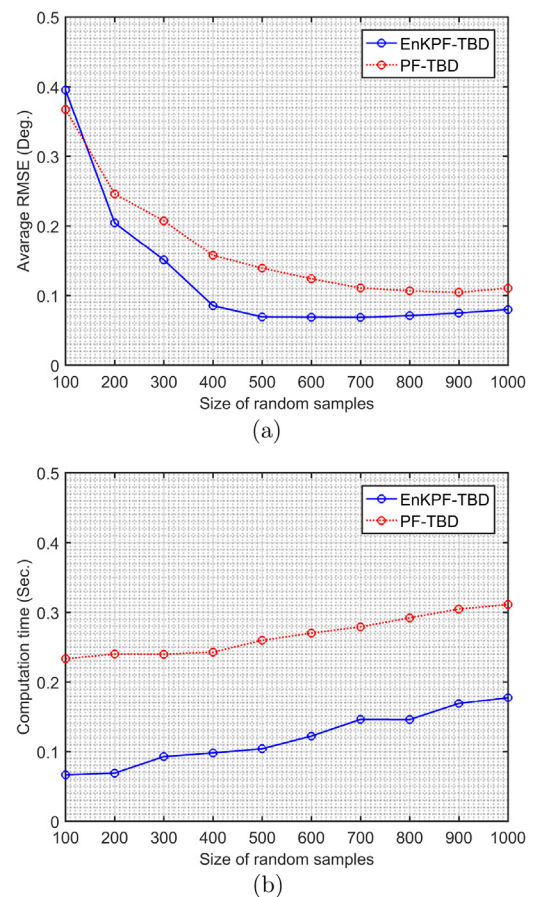


Fig. 7. Performance comparison of EnKPF-TBD and PF-TBD non-parametric techniques, showing (a) estimation accuracy (average RMSE) and (b) computation time for differently sized random samples, i.e., [100, 1000], respectively.

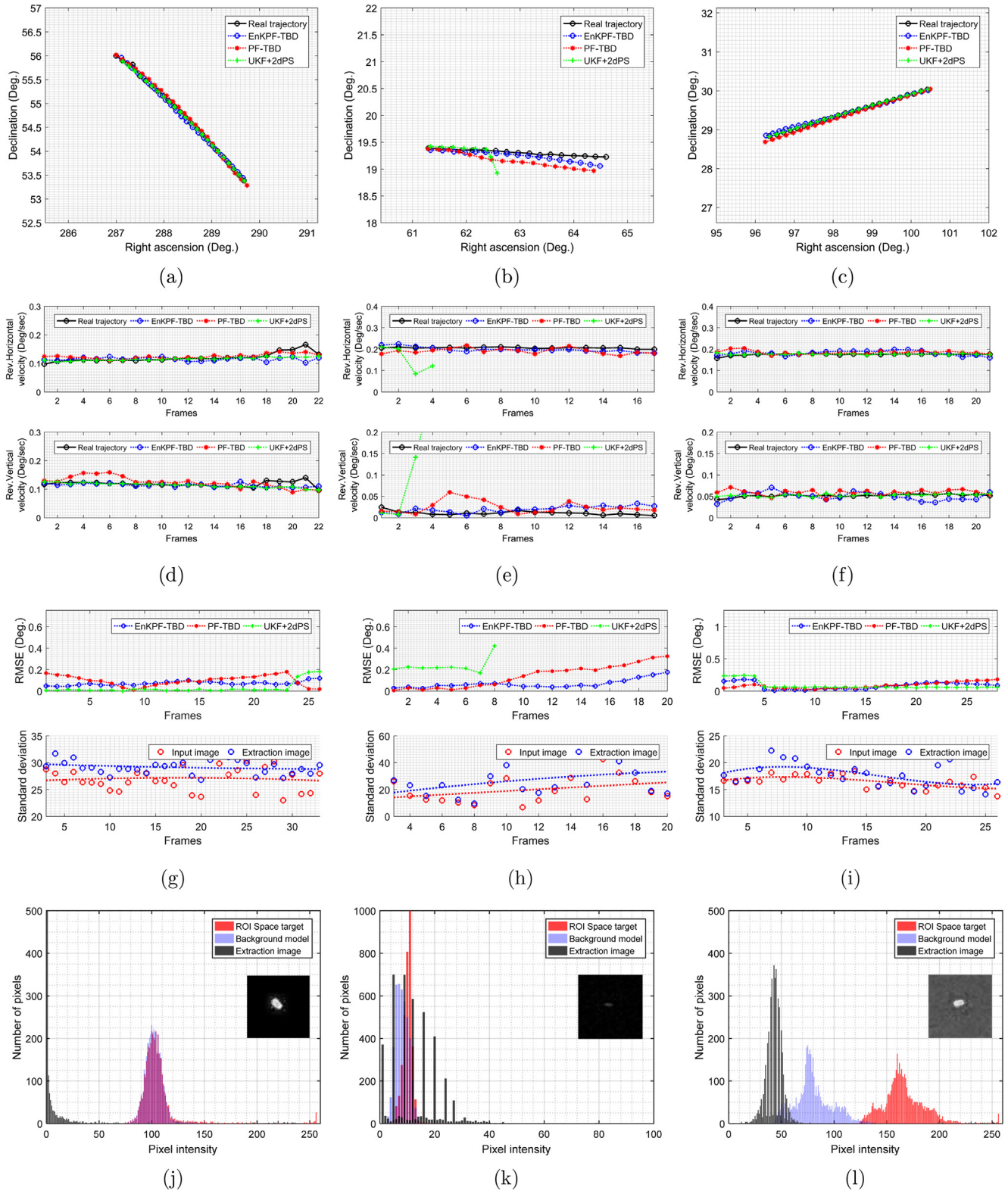


Fig. 8. (a)–(i) Comparison of tracking performances of three TBD baseline frameworks (EnKPF-TBD, PF-TBD, and UKF+2dPS) for three primary datasets (Datasets A–C). (j)–(l) Image histograms between input image, background model, and extraction image based on RGA approach for 64×64 pixel² ROI around space target. The ROI-based extraction images are located on the top right of the image histograms.

≈ 175 yielded average RMSEs of 0.0728, 0.0977, and 0.0490 deg, respectively. The most striking observation from this comparison is that the UKF + 2dPS technique

works well following definition of the appropriate threshold through trial and error. This is because the 2dPS mechanism searches for the peak location (single point) more

efficiently when the target intensity is sufficiently light and appears on a clear-sky background. However, the non-threshold-based TBD frameworks use Eq. (16) to calculate the likelihood weights with respect to the target amplitude and nearest pixels of background noise. In the second tracking validation, we used Dataset B (a small and dim space target). The tracking performance results are presented in Fig. 8(b), (e), and (h), respectively. It is evident that the UKF + 2dPS technique with a background interference threshold of ≈ 35 works well for the first tracking time period. This is because the close difference between the target and background intensities causes diversion of the UKF + 2dPS tracking result. For EnKPF-TBD and PF-TBD, tracking continued under this condition with average RMSEs of 0.0749 and 0.1511 deg, respectively. In other words, EnKPF-TBD incorporating the KF approach can reduce the tracking error to approximately half that of the PF-TBD. Finally, for Dataset C, the dynamic background case, the fitted data (red and blue dashed lines) exhibit a dynamic trend with variation of the σ^2 clutter level before and after extraction processing, as shown in the lower section of Fig. 8(i). The object path is shown in Fig. 8(c). After appropriately updating $\delta_{i(x,y)}^{(x,y)}$, the two TBD baseline frameworks and UKF + 2dPS could continuously track the object under this condition with average RMSEs of 0.0841, 0.0882, and 0.0867 deg for EnKPF-TBD, PF-TBD, and UKF + 2dPS, respectively, with a background interference threshold of ≈ 200 . To determine the robustness of the proposed approaches, we did not adjust the initial parameters in the new environment. Normally, the sensitivity and standard deviation of the tracking error for a small and dim target are higher than those for a bright target. However, the proposed EnKPF-TBD can achieve both position accuracy and efficiency within the computation time; these are important characteristics for autonomous tracking of a moving space target. However, the state-of-the-art approach combines information from measurement sensors with a kinematic model of the considered system to predict its states. This is a fundamental problem of state estimation techniques, as the kinematic model is considered completely known a priori. Taking the tracking frameworks under all circumstances as an example, the shape of the space target appearing on the screen should only be in the PSF; therefore, the proposed frameworks perform well only for a short exposure time.

5. Conclusion

In this article, we presented novel techniques to overcome the problems hindering realization of autonomous PO-based space target tracking, an objective for the development of modern ground-based space surveillance networks. In particular, although significant progress has been made in the field of astrometry in recent years, non-linear and/or non-Gaussian estimation remains a challenging problem. The propose of this study was to develop

techniques combining image processing and state estimation based on TBD frameworks to detect small and dim targets, and to improve their capability to maintain robust tracking against a dynamic background.

The proposed methods include two main steps. The first is autonomous determination of the initial orbit trajectory, in which we apply LI integrated with 2dPS detection to guide the TBD frameworks. Our experiment results show that this combined approach not only reduces the effect of the background interference, but also improves the space target contrast, which can increase the probability of target detection in the initial state. In the proposed technique, the first procedure is then integrated with the second tracking stage, for which a novel EnKPF-TBD algorithm was developed to reduce the effect of particle degeneracy and the computational cost of PF-TBD. In this work, two non-parametric TBD frameworks (EnKPF-TBD and PF-TBD) and threshold-based UKF-2dPS tracking were considered. To verify their effectiveness, three real astronomical image datasets acquired by an APOSOS telescope, for a normal-sky background, small and dim space target, and highly dynamic background, were used to evaluate the new algorithm. The results demonstrate that the proposed EnKPF-TBD combination algorithm yields considerable improvement in tracking accuracy, precision, and robustness compared to the other methods in all examined situations. In particular, the random sample size is far smaller than that of the PF-TBD; therefore, use of the EnKPF-TBD can decrease the computational demand of the tracking method and render it more suitable for real-world application. In future work, we will continue to develop multiple target tracking implementations and design a closed-loop control for a robotic telescope system.

Acknowledgments

The authors are thankful for fellowship support from The World Academy of Sciences (TWAS), the Chinese Academy of Sciences (CAS), and the Asia-Pacific Space Cooperation Organization (APSCO). Funding for this study was provided, in part, by National Research and Development Projects for Key Scientific Instruments, Grant No. ZDYZ2013-2, and through a key project supported by the Bureau of International Cooperation, CAS, contract No. 181811KYSB20170018. Finally, the authors are also grateful to the reviewers for their detailed reviews, constructive comments, and suggestions.

References

- Adurthi, N., Singla, P., Majji, M., 2014. Conjugate unscented transformation based orbital state estimation and sensor tasking for efficient space surveillance. In: AIAA/AAS Astrodynamics Specialist Conference.
- Benoudnine, H., Meche, A., Keche, M., Ouamri, A., Woolfson, M.S., 2016. Real time hough transform based track initiators in clutter. Inf. Sci. 337 (C), 82–92.

- Bi, H., Ma, J., Wang, F., 2015. An improved particle filter algorithm based on ensemble Kalman filter and Markov Chain Monte Carlo method. *IEEE J. Sel. Top. Appl. Earth Obser. Remote Sens.* 8 (2), 447–459.
- Bocquet, M., Pires, C.A., Wu, L., 2010. Beyond gaussian statistical modeling in geophysical data assimilation. *Mon. Weather Rev.* 138 (8), 2997–3023.
- Boers, Y., Driessen, H., Torstensson, J., Trieb, M., 2006. Track-before-detect algorithm for tracking extended targets. *Radar, Sonar Navigat., IEE Proc.* 153 (4), 345–351.
- Chee, S.A., Forbes, J.R., 2016. Norm-constrained unscented Kalman filter with application to high area-to-mass ratio space-debris tracking. In: *AIAA Guidance, Navigation, and Control Conference*.
- Duan, H., Deng, Y., Wang, X., Xu, C., 2013. Small and dim target detection via lateral inhibition filtering and artificial bee colony based selective visual attention. *Plos One* 8 (8), e72035.
- Evensen, G., 2003. The ensemble Kalman filter: theoretical formulation and practical implementation. *Ocean Dyn.* 53 (4), 343–367.
- Fang, H., Tian, N., Wang, Y., Zhou, M., Haile, M.A., 2018. Nonlinear Bayesian estimation: from Kalman filtering to a broader horizon. *IEEE/CAA J. Autom. Sinica* 5 (2), 401–417. <https://doi.org/10.1109/JAS.2017.7510808>.
- Gordon, N.J., Salmond, D.J., Smith, A.F.M., 1993. Novel approach to nonlinear/non-gaussian bayesian state estimation. *IEE Proc. F Radar Signal Process.* 140 (2), 107–113.
- Huang, J., Hu, W., 2014. Mcmc-particle-based group tracking of space objects within bayesian framework. *Adv. Space Res.* 53 (2), 280–294.
- Insom, P., Cao, C., Boonsrimuang, P., Torteeka, P., Boonprong, S., Liu, D., Chen, W., 2017. The dynamics of wetland cover change using a state estimation technique applied to time-series remote sensing imagery. *Geomat. Natl. Hazards Risk*, 1–16.
- Julier, S.J., Uhlmann, J.K., 2004. Unscented filtering and nonlinear estimation. *Proc. IEEE* 92 (3), 401–422.
- Kenney, C.S., Zuliani, M., Manjunath, B.S., 2005. An axiomatic approach to corner detection. In: *IEEE Computer Society Conference on Computer Vision and Pattern Recognition*, pp. 191–197.
- Kessler, D.J., Johnson, N.L., Liou, J., Matney, M., 2010. The Kessler syndrome: implications to future space operations. *Adv. Astronaut. Sci.* 137 (8), 2010.
- Kovalevsky, J., Seidelmann, P.K., 2004. *Fundamentals of Astrometry*. Cambridge University Press.
- Li, L., Li, Y., 2017. Particle filter track-before-detect algorithm with lamarckian inheritance for improved dim target tracking. In: *Evolutionary Computation*.
- Liu, J.J.F., 1987. Norad satellite tracking. In: *NASA Conference Publication*.
- Mikolajczyk, K., Schmid, C., 2004. Scale and affine invariant interest point detectors. *Int. J. Comput. Vision* 60 (1), 63–86.
- Murphy, T.S., Holzinger, M.J., Flewelling, B., 2016. Space object detection in images using matched filter bank and Bayesian update, 1–13.
- Nagarajan, K., Judge, J., Graham, W.D., Monsivais-Huetero, A., 2011. Particle filter-based assimilation algorithms for improved estimation of root-zone soil moisture under dynamic vegetation conditions. *Adv. Water Resour.* 34 (4), 433–447.
- Ng, K.K., Delp, E.J., 2010. Object tracking initialization using automatic moving object detection. In: *IS&T/SPIE Electronic Imaging*. International Society for Optics and Photonics, pp. 75430M–75430M.
- Pelton, J.N., 2017. *Tracking of Orbital Debris and Avoidance of Satellite Collisions*. Springer International Publishing.
- Piattoni, J., Ceruti, A., Piergentili, F., 2014. Automated image analysis for space debris identification and astrometric measurements. *Acta Astronaut.* 103, 176–184.
- Robert, S., Knsch, H.R., 2016. Localizing the ensemble Kalman particle filter.
- Rollason, M., Salmond, D., 2001. A particle filter for track-before-detect of a target with unknown amplitude. *Target Tracking: Algorithms and Applications*, vol. 1, pp. 14/1–14/4.
- Salmond, D., Birch, H., 2001. A particle filter for track-before-detect. *American Control Conference*, 2001. Proceedings of the 2001, vol. 5. IEEE, pp. 3755–3760.
- Shen, Zheqi, Zhang, Xiangming, Tang, Youmin, 2016. Comparison and combination of eakf and sir-pf in the Bayesian filter framework. *Acta Oseanol. Sin.* 35 (3), 69–78.
- Shen, Z., Tang, Y., 2015. A modified ensemble Kalman particle filter for non-Gaussian systems with nonlinear measurement functions. *J. Adv. Model. Earth Syst.* 7 (1).
- Space, Scientific and Technical Subcommittee of the United Nations Committee on the Peaceful Uses of Outer. 1999. *Technical Report on Space Debris. (in Chicago citation style)*.
- Sun, R.Y., Zhan, J.W., Zhao, C.Y., Zhang, X.X., 2015. Algorithms and applications for detecting faint space debris in geo. *Acta Astronaut.* 110, 9–17.
- Tang, Z., Miao, Z., Wan, Y., 2007. Background subtraction using running gaussian average and frame difference. In: *International Conference on Entertainment Computing*, pp. 411–414.
- Torteeka, P., Gao, P.Q., Shen, M., Guo, X.Z., Yang, D.T., Yu, H.H., Zhou, W.P., Zhao, Y., 2017a. A robust space debris tracking strategy based on multiple-model particle filter via aposos telescope. In: *Global Space Exploration Conference*.
- Torteeka, P., Gao, P.Q., Shen, M., Guo, X.Z., Yang, D.T., Yu, H.H., Zhou, W.P., Zhao, Y., 2017b. Space debris tracking based on fuzzy running gaussian average adaptive particle filter track-before-detect algorithm. *Res. Astron. Astrophys.* 17 (2), 51–62.
- Virtanen, J., Poikonen, J., Sääntti, T., Komulainen, T., Torppa, J., Granvik, M., Muinonen, K., Pentikäinen, H., Martikainen, J., Näränen, J., et al., 2016. Streak detection and analysis pipeline for space-debris optical images. *Adv. Space Res.* 57 (8), 1607–1623.
- Wren, C.R., Azarbayejani, A., Darrell, T., Pentland, A.P., 1996. Pfindex: real-time tracking of the human body. In: *International Conference on Automatic Face and Gesture Recognition*, pp. 51–56.
- Ye, T., Zhou, F., 2015. Autonomous space target recognition and tracking approach using star sensors based on a Kalman filter. *Appl. Opt.* 54 (11), 3455–3469.